



## NRC Publications Archive Archives des publications du CNRC

### **Enhanced terahertz transmission through bullseye plasmonics lenses fabricated using micromilling techniques**

Heggie, Tanner J.; Naylor, David A.; Gom, Brad G.; Bordatchev, Evgueni; Trimboli, M. Grace

This publication could be one of several versions: author's original, accepted manuscript or the publisher's version. / La version de cette publication peut être l'une des suivantes : la version prépublication de l'auteur, la version acceptée du manuscrit ou la version de l'éditeur.

For the publisher's version, please access the DOI link below. / Pour consulter la version de l'éditeur, utilisez le lien DOI ci-dessous.

#### **Publisher's version / Version de l'éditeur:**

<https://doi.org/10.1007/s11468-015-0152-7>

*Plasmonics*, 2016-01-06

#### **NRC Publications Record / Notice d'Archives des publications de CNRC:**

<https://nrc-publications.canada.ca/eng/view/object/?id=f1db54cc-4523-433e-b903-20384f8da672>

<https://publications-cnrc.canada.ca/fra/voir/objet/?id=f1db54cc-4523-433e-b903-20384f8da672>

Access and use of this website and the material on it are subject to the Terms and Conditions set forth at

<https://nrc-publications.canada.ca/eng/copyright>

READ THESE TERMS AND CONDITIONS CAREFULLY BEFORE USING THIS WEBSITE.

L'accès à ce site Web et l'utilisation de son contenu sont assujettis aux conditions présentées dans le site

<https://publications-cnrc.canada.ca/fra/droits>

LISEZ CES CONDITIONS ATTENTIVEMENT AVANT D'UTILISER CE SITE WEB.

#### **Questions?** Contact the NRC Publications Archive team at

PublicationsArchive-ArchivesPublications@nrc-cnrc.gc.ca. If you wish to email the authors directly, please see the first page of the publication for their contact information.

**Vous avez des questions?** Nous pouvons vous aider. Pour communiquer directement avec un auteur, consultez la première page de la revue dans laquelle son article a été publié afin de trouver ses coordonnées. Si vous n'arrivez pas à les repérer, communiquez avec nous à PublicationsArchive-ArchivesPublications@nrc-cnrc.gc.ca.



# Enhanced Terahertz Transmission Through Bullseye Plasmonics Lenses Fabricated Using Micromilling Techniques

Tanner J. Heggie<sup>1</sup> · David A. Naylor<sup>1</sup> · Brad G. Gom<sup>1</sup> · Evgueni Bordatchev<sup>2</sup> · M. Grace Trimboli<sup>1</sup>

Received: 11 September 2015 / Accepted: 11 December 2015  
© Springer Science+Business Media New York 2016

**Abstract** Imaging applications at terahertz frequencies are, in general, limited to relatively low spatial resolution due to the effects of diffraction. By using a subwavelength aperture in the near-field, however, it is possible to achieve subwavelength resolution, although low transmission through the aperture limits the sensitivity of this approach. Plasmonic lenses in the form of bullseye structures, which consist of a circular subwavelength aperture surrounded by concentric periodic corrugations, have demonstrated enhanced transmission, thereby increasing the utility of near-field imaging configurations. In this paper, the design, fabrication, and experimental performance of plasmonic lenses optimized for 300 GHz are discussed. While nanofabrication techniques are required for optical applications, microfabrication techniques are sufficient for terahertz applications. The process flow for fabricating a double-sided bullseye structure using a precision micromilling technique is described. Transmission and beam profile measurements using a customized terahertz testbed are presented.

**Keywords** Terahertz · Plasmonic lens · Bullseye · Microfabrication · Enhanced transmission

## Introduction

In recent years, there has been growing interest in the use of terahertz (THz) radiation as a diagnostic tool for differentiating between fat, muscular, and cancerous tissue [1, 2]. The greatest difference in the absorption of cancerous tissue, when compared with healthy tissue, occurs at frequencies around 300 GHz [3]; however, the effects of diffraction limit the attainable spatial resolution to the order of the wavelength, in this case  $\lambda \approx 1$  mm [4]. By using a subwavelength aperture in a near-field configuration, the spatial resolution can be improved, albeit at the cost of lower transmission [5]. For example, in an infinitesimally thin perfect electrical conductor in the extreme subwavelength regime ( $kr \ll 1$ ), the transmitted power through a circular aperture scales as  $r^6/\lambda^4$ , where  $k = 2\pi/\lambda$ ,  $r$  is the aperture radius, and  $\lambda$  is the wavelength of the incident light [6]. Since typical THz sources have low power, the low transmission through a subwavelength aperture limits the utility of THz subwavelength imaging unless sensitive, cryogenically-cooled detector systems are employed.

The discovery of extraordinary transmission (EOT) of light through subwavelength hole arrays by Ebbesen et al. [7] has been attributed to the presence of surface plasmon polaritons (SPP), arising when electromagnetic waves incident from a dielectric medium couple to the oscillation of free charge carriers near the surface of a conductor [8]. Since the discovery, there has been a rapid development in the design of devices that exploit the properties of SPP. SPP can be resonantly excited by a periodic grating,

---

✉ Tanner J. Heggie  
tanner.heggie@uleth.ca

David A. Naylor  
naylor@uleth.ca

Evgueni Bordatchev  
evgueni.bordatchev@nrc-cnrc.gc.ca

<sup>1</sup> Department of Physics and Astronomy, University of Lethbridge, 4401 University Dr W, Lethbridge, AB, Canada T1K 6T5

<sup>2</sup> NRC Automotive & Surface Transportation, London, ON, Canada

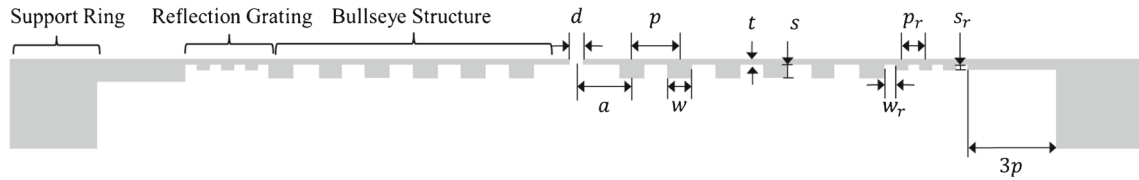


**Fig. 1** A cross-sectional view of a single-sided BE lens of aperture diameter,  $d$ , and thickness,  $t$ . The geometry of the coupling structure is parametrized by its periodicity,  $p$ , ring width,  $w$ , ring depth,  $s$ , and the distance to first ring,  $a$ . The Bragg reflection grating is similarly

parametrized by its period,  $p_r$ , width,  $w_r$ , and depth,  $s_r$ . The device has a full diameter of 25 mm and is surrounded by a support ring with a height of 2 mm

the efficiency of which is directly related to the geometrical parameters of the grating structure. With the goal of increasing the data packing density of optical data recording structures, studies of EOT have primarily focused on applications at visible wavelengths to enhance transmission through subwavelength metallic hole arrays, slits, and bullseye (BE) lenses [7, 9, 10]. A similar gain in transmission can be achieved at THz frequencies by optimizing the grating parameters for this region.

The BE lens consist a circular aperture surrounded by concentric corrugations on the input and/or output surface of the metal (Fig. 1). Structures on the input side of a BE lens serve to couple the incident radiation field to SPP, which propagate along the surface of the lens and lead to enhanced fields above the aperture. As a result, the transmitted power is over an order of magnitude larger than predicted from classical diffraction theory. An additional transmission enhancement has been observed by placing a half-period Bragg grating outside the principle bullseye structure. The Bragg grating serves to reflect the outward traveling SPP, further enhancing the field above the aperture [11]. Structures on the output side of a BE lens serve to couple the SPP to the radiation field [10]. Phase delays induced by the output structure lead to interference effects that can, in principle, be tailored to effectively focus the emerging beam [12, 13].

This paper presents the design, fabrication, and verification of THz BE lenses with input geometry chosen for enhanced transmission at 325 GHz, and an output geometry chosen to focus the emerging beam at a distance of 3 mm.

**Theory**

The characteristic length scales of SPP, namely the metallic skin depth,  $\delta_m$ , dielectric skin depth,  $\delta_d$ , and the propagation

length along the interface,  $L$ , are derived from components of the SPP wave vector,  $\mathbf{k}$  [14, 15]. Parallel to the interface,

$$k_x = k'_x + ik''_x = k_0 \sqrt{\frac{\epsilon_d \epsilon_m}{\epsilon_d + \epsilon_m}}, \tag{1}$$

where  $k_0$  is the free space wave vector,  $\epsilon_d$  is the relative permittivity of the dielectric, and  $\epsilon_m$  is the complex relative permittivity of the metal. The propagation length  $L = 1/2k''_x$  is the distance parallel to the interface that the intensity of the electromagnetic field drops by  $1/e$ .

Perpendicular to the interface, the  $z$ -component of the wave vector towards the metal is given by:

$$k_{zm} = k'_{zm} + ik''_{zm} = \sqrt{\epsilon_m k_0^2 - k_x^2}. \tag{2}$$

The metallic skin depth,  $\delta_m = 1/k''_{zm}$ , is defined as the distance normal to the interface where the field amplitude decreases by a factor of  $1/e$ . An analogous equation exists for the  $z$ -component of the wave vector into the dielectric,

$$k_{zd} = k'_{zd} + ik''_{zd} = \sqrt{\epsilon_d k_0^2 - k_x^2}, \tag{3}$$

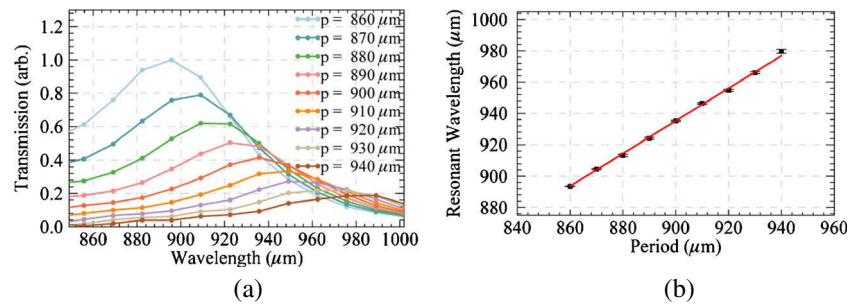
and  $\delta_d = 1/k''_{zd}$  is the dielectric skin depth.

By way of illustration, the characteristic lengths of SPP on a Au-air interface, calculated in the visible ( $\lambda = 632.8$  nm) and in the THz ( $\lambda = 922$   $\mu$ m) regions, are presented in Table 1. A multi-coefficient model [16] was used to fit Au permittivity data from Johnson and Christy [17] for  $\lambda \in [500$  nm, 700 nm], yielding  $\epsilon_m = -11.7 + i1.2$  at  $\lambda = 632.8$  nm. For noble metals at visible wavelengths, SPP are typically characterized, with respect to the wavelength, by a strong confinement of their electromagnetic fields near the surface, a relatively large penetration distance within the metal, and moderately long propagation lengths.

**Table 1** The skin depth in the metal,  $\delta_m$ , skin depth in the dielectric,  $\delta_d$ , and propagation length,  $L$ , of visible and THz SPP on a Au-air interface

	$\lambda$ (m)	$\delta_m$ (m)	$\delta_d$ (m)	$L$ (m)
Visible SPP	$6.33 \times 10^{-7}$	$3.00 \times 10^{-8} \approx 10^{-2}\lambda$	$3.00 \times 10^{-7} \approx 0.5\lambda$	$1.00 \times 10^{-5} \approx 16\lambda$
THz SPP	$9.22 \times 10^{-4}$	$1.35 \times 10^{-7} \approx 10^{-4}\lambda$	$3.00 \times 10^{-1} \approx 10^2\lambda$	$3.30 \times 10^2 \approx 10^5\lambda$

**Fig. 2** **a** The variation in transmission with wavelength for bullseye lenses having different periods. **b** The variation in resonant wavelength with the grating period

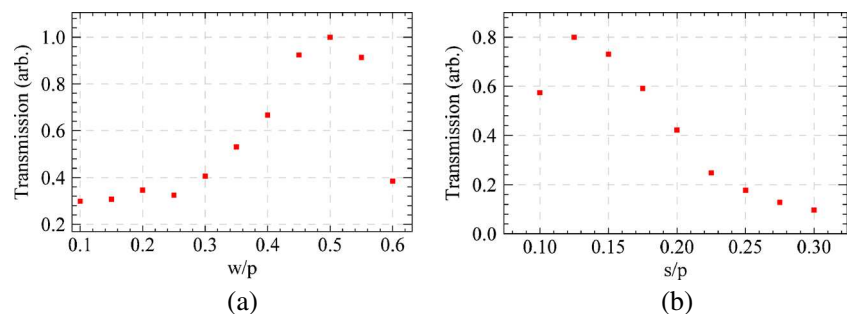


**THz Plasmonics**

Compared to visible wavelengths, THz permittivity values are typically 5–6 orders of magnitude larger. Using the Drude model and parameters given by Ordal et al. [18], the permittivity of Au at 325 GHz is  $\epsilon_m = -1.12 \times 10^5 + i2.24 \times 10^6$ . Repeating the above analysis, THz SPP extend far into the dielectric medium, have relatively small metallic skin depth, and have propagation lengths many orders of magnitude larger than the wavelength (Table 1).

It is worth noting that while the SPP length scales at optical wavelength vary significantly from one metal to another, at THz frequencies, the permittivity of most metals approach that of perfect electrical conductors. The choice of material can therefore be based on other parameters, such as machinability, cost, etc. Furthermore, since only the material properties within approximately one skin depth contribute significantly to the operation of a plasmonic device, plasmonic devices operating at THz frequencies can be made thin, with correspondingly greater transmission [19]. While THz BE lenses have been made using lithographic and chemical fabrication techniques, this requires access to a nano-fabrication facility [11, 19, 20]. In addition, the self-masking of the structure makes it challenging to achieve a relatively large and uniform deposition depth with a lithographic technique. Since the required precision of a THz plasmonic device scales with wavelength, it is possible to achieve the same relative accuracy at THz frequencies using a micromachining approach. In Section “Fabrication”, we present a novel precision micromachining approach for the fabrication of BE lenses.

**Fig. 3** The variation in transmission at  $\lambda = 922 \mu\text{m}$  as the ring width,  $w$  and ring depth,  $s$  are varied



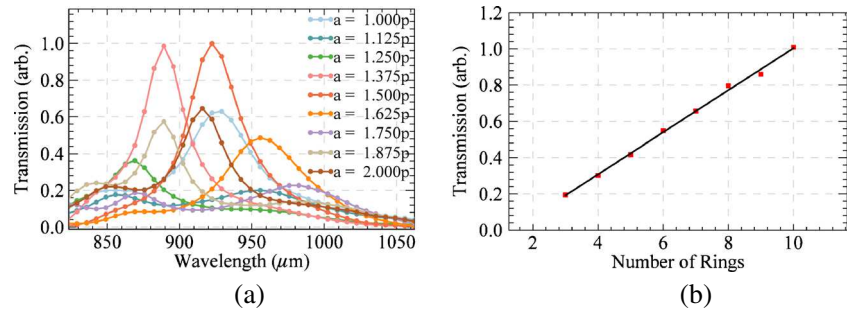
**Theoretical Modeling**

The transmission through a BE lens can be considered in terms of three independent components: (1) the coupling of incident light into SPP, (2) the evanescent transmission through the aperture, and (3) the coupling of SPP back into the radiation field [8].

**Input Coupling**

Numerical and experimental studies have demonstrated that the efficiency of coupling light incident on a BE lens into SPP is primarily dictated by the grating period,  $p$  [21]. Other interconnected structural parameters, such as the ring width,  $w$ , ring depth,  $s$ , and the distance to the first ring,  $a$ , also play a role and their values can be optimized to yield maximum transmission (Fig. 1). At visible wavelengths, rules of thumb have been developed to aid in the design of a BE lens with a transmission resonance at  $\lambda_R$ :  $p = 1.1\lambda_R$ ,  $w/p = 0.5$ ,  $s/p = 0.2$ , and  $a = p/2$  [21]. These relationships were used as a starting point for modeling the performance of THz BE lenses at  $\lambda_R = 922 \mu\text{m}$  (325 GHz). Since the permittivity values in the visible and THz are significantly different, each parameter was varied in turn to determine the scale laws appropriate for THz frequencies. A commercial simulator based on the finite-difference time-domain method was used to optimize the transmission gain,  $G = T_{be}/T_{ap}$ , defined as the ratio of the power exiting the BE lens,  $T_{be}$ , and that through an aperture having identical thickness and diameter,  $T_{ap}$  [16].

**Fig. 4** **a** The variation in transmission as a function of the distance to the first ring,  $a$ . Larger transmission resonances were observed when  $a$  was an odd half-multiple of the period. **b** The variation in transmission as the number of rings increases



A numerical mesh was adopted that was appropriate to the spatial dimensions of the lens. In the transmission direction,  $z$ , a mesh size on the order of tens of microns is required to accommodate the small depth of the structures, while in the transverse  $xy$ -direction structures are on the scale of order of the hundreds of microns and a larger mesh size can be used. As a starting point, a numerical mesh of 10  $\mu\text{m}$  was chosen for all directions. Simulations were repeated using finer meshes in each direction until the simulated transmission values converged to within 5%. It was found that converged simulations required mesh sizes of  $\Delta z = 4 \mu\text{m}$  and  $\Delta x = \Delta y = 19 \mu\text{m}$ . Simulations with these mesh parameters required 1.5 h to run with an Intel Xeon X5680 64-Bit, 3.33 GHz processor with 24 cores and 50 GB RAM.

The results of the optimization process, in which the transmission has been plotted as a function of the variable under consideration, are shown in Figs. 2, 3, and 4. Figure 2a shows the variation in transmission as a function of wavelength for different periods. In Fig. 2b, this information is distilled to show the resonant wavelength,  $\lambda_R$ , as a function of the grating period. A linear relationship is observed given by  $\lambda_R = (1.038 \pm 0.001)p$ . Figure 3 shows the optimum width-to-period and depth-to-period ratios when the incident radiation is fixed at design wavelength of 922  $\mu\text{m}$ . A resonance is observed with the optimum parameters of  $w/p = 0.499 \pm 0.001$  and  $s/p = 0.14 \pm 0.01$ , where the errors represent the uncertainty determined from parabolic fits to the resonance peaks in Fig. 3. The optimum starting ring distances takes the form of  $a = (2m + 1)p/2$

( $m = 0, 1, 2, \dots$ ), as shown in Fig. 4a. Furthermore, in contrast to visible applications where increasing the number of rings beyond a certain point does not lead to increased transmission, at THz frequencies Fig. 4b shows that transmission continues to increase with the number of rings. This result can be explained by the differences in the propagation length, as given in Table 1. This allows THz BE lenses to be made arbitrarily large to increase the coupling area and thus the transmission gain.

These theoretical results can be compared directly with the rules of thumb established for visible wavelengths. While the width-to-period and the distance to first ring (for  $m = 0$ ) are similar, the relationships for the resonant wavelength to period and depth-to-period are found to be significantly different. These modified rules of thumb should be adopted for designing BE lenses at THz frequencies.

Since the propagation length,  $L$ , at THz frequencies, is extremely large (Table 1), an additional gain can be realized by using a Bragg reflection grating, consisting of half-period concentric rings placed outside of the main BE structure, as shown in Fig. 1 [11]. The Bragg grating serves to reflect, in phase, SPP back towards the central circular aperture, thereby increasing the resulting field at the aperture location. The Bragg reflector of dimensions given in Table 2 resulted in an additional simulated transmission gain of 25%. At the same time, it was noted that the peak wavelength shifted to 915  $\mu\text{m}$ , which we believe is due to a small residual phase error introduced by the Bragg reflector.

**Table 2** The designed and fabricated dimensions (Fig. 1) of the two single-sided BE devices, SS1 and SS2, and the double-sided radially tuned device, DS1

	$d$ ( $\mu\text{m}$ )	$t$ ( $\mu\text{m}$ )	$a$ ( $\mu\text{m}$ )	$p$ ( $\mu\text{m}$ )	$w$ ( $\mu\text{m}$ )	$s$ ( $\mu\text{m}$ )	$p_r$ ( $\mu\text{m}$ )	$w_r$ ( $\mu\text{m}$ )	$s_r$ ( $\mu\text{m}$ )
Design 1	300.0	50.0	1332.0	888.0	444.0	130.0	444.0	222.0	65.0
SS1	299.8	48.6	1336.4	890.4	445.2	129.0	448.8	224.4	66.6
DS1	298.8	37.4	1334.9	891.8	445.9	130.2	447.0	223.5	66.1
Design 2	200.0	30.0	1332.0	888.0	444.0	130.0	444.0	222.0	65.0
SS2	198.8	20.0	1331.5	884.0	442.0	124.0	444.0	222.0	57.5

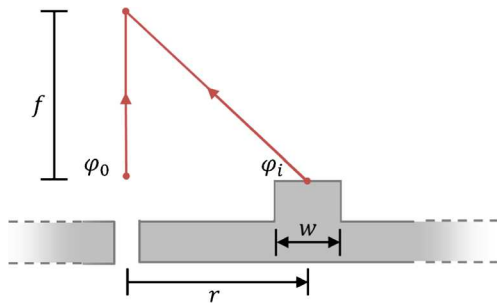


**Fig. 5** The simulated phase was recorded at the top of the ring and at the center of the aperture in the plane defined by the top of the ring. Simulations were performed by varying the width and radius of the ring

**Transmission Through the Aperture**

From classical theory, the transmission of light through a circular aperture decays exponential with material thickness and is well described using a cylindrical model for  $d \leq 0.586\lambda$  [22]. For example, an aperture with a diameter of  $d = 200 \mu\text{m}$ , which represents one of our fabricated devices, has an attenuation constant of  $\alpha = 17.09 \text{ mm}^{-1}$  at  $\lambda = 922 \mu\text{m}$ . As described in Section “Fabrication”, we were able to fabricated this device with a thickness of  $20 \mu\text{m}$ , which is within a factor of 2 of the limiting transmission possible with a infinitesimally thin device. The minimum achievable thickness possible with micromachining techniques therefore does not place a serious limitation on the production of efficient THz plasmonic devices.

**Output Coupling**

Structures on the output side of the lens can collimate or focus the emerging beam. This has been shown by mirroring the input corrugations to the output surface [10, 23, 24] and by modulating the radial position [25] or depths of the surface structure [26–28]. Phenomenological phase modulation models have been developed for nano-scaled slit-groove devices and BE lenses [12, 13, 29]. In these simple models, SPP excited on the output side of the lens propagate along the surface, scatter off output surface structures, and subsequently couple back to the radiation field. Individual

corrugations can be thought of as a Huygen emitter with a specific initial phase,  $\varphi_i$ . The relative phase difference,  $\varphi_{i,0}$ , between light traveling through the central aperture,  $\varphi_0$ , and that of SPP scattered off surface corrugations,  $\varphi_i$ , can be found using numerical techniques.

For constructive interference at a focal distance,  $f$ , the phase difference due to SPP scattering off a ring at radius  $r$ , as shown in Fig. 5, must satisfy:

$$\left(\sqrt{f^2 + r^2} - f\right)k + \varphi_{i,0} = 2\pi m, m = 0, \pm 1, \pm 2, \dots \quad (4)$$

To investigate the variation in the phase of the secondary sources as a function of ring radius and width, simulations were performed at  $\lambda = 922 \mu\text{m}$  for an aperture diameter of  $300 \mu\text{m}$  and thickness of  $50 \mu\text{m}$ . As an example, a single ring with a width of  $445 \mu\text{m}$  and a height of  $130 \mu\text{m}$  was placed on the output side of the device and its radial position allowed to vary. This principle is illustrated in Fig. 5. The phases at the location of the ring and the aperture were recorded to find the phase difference  $\varphi_{i,0}$  as a function of  $r$ . The raw simulated data are shown in Fig. 6a. As expected, the phase difference  $\varphi_{i,0}$  increases linearly as a function of ring radius and is wrapped around  $\pm\pi$ . After unwrapping the phase (Fig. 6b), a linear fit to the date yielded a slope and intercept of  $m_r = 6.8 \pm 0.1 \text{ mm}^{-1}$  and  $b_r = -2.9 \pm 0.1$ , respectively.

A single ring was then simulated at radii of  $r = 700, 1150, \text{ and } 2500 \mu\text{m}$  for different widths. Following a similar procedure, linear fits gave an average slope of  $m_w = -3.5 \pm 0.3 \text{ mm}^{-1}$  and intercepts of  $b_w = 9.8 \pm 0.1, b_w = 6.4 \pm 0.1, b_w = 9.4 \pm 0.1$ , corresponding to the three radial positions given above.

It is reasonable to express the total phase  $\varphi_{i,0}$  as the sum of the individual contributions due to each structural parameter:

$$\varphi_{i,0} = \varphi_r + \varphi_w, \quad (5)$$

where  $\varphi_r = m_r r + b_r$  and  $\varphi_w = m_w w + b_w$ . Combining terms, the total phase can be expressed as

$$\varphi_{i,0} = m_r r + m_w w + b, \quad (6)$$

where  $m_r = 6.8 \pm 0.1 \text{ mm}^{-1}, m_w = -3.5 \pm 0.3 \text{ mm}^{-1}$ , and  $b = b_r + b_w = -1.3 \pm 0.1$ . Using the output ring

**Fig. 6 a** The phase difference between light transmitted through a  $d = 200 \mu\text{m}$  aperture,  $\varphi_0$ , and that light scattered off a ring having a  $s = 100 \mu\text{m}$ ,  $w = 445 \mu\text{m}$  at increasing radial distances. **b** The unwrapped phase difference fitted with a linear function

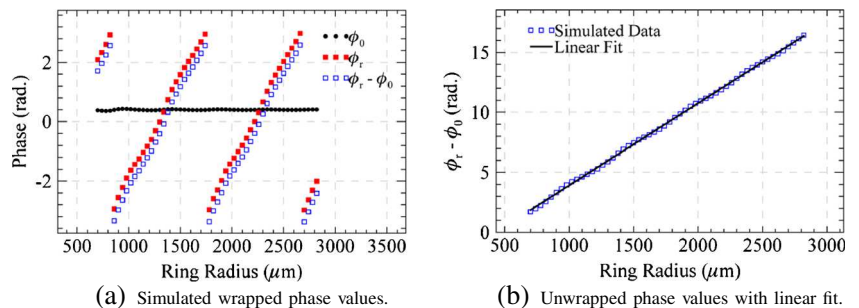
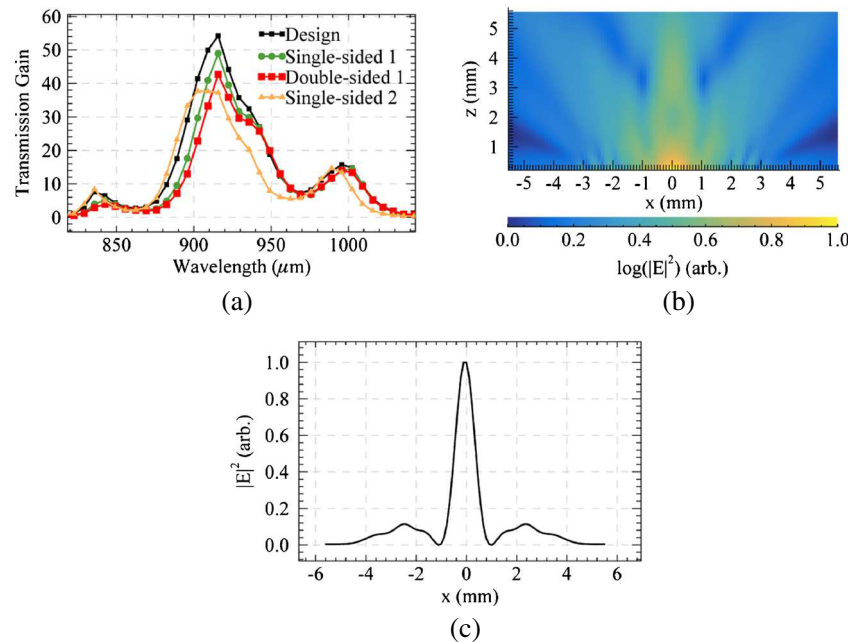


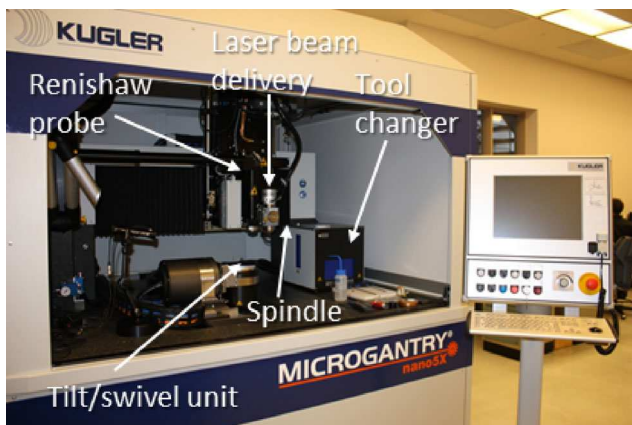
**Fig. 7** **a** A comparison of the simulated transmission gain for the designed and as-built lenses with dimensions given in Table 2. **b** The simulated beam profile of DS1, designed to have a focus 3 mm behind the lens. **c** Cross section of the beam profile through the minimum waist at  $z = 3.2$  mm, demonstrating beam confinement



phase relation, ring radii were generated for a wavelength of 922  $\mu\text{m}$  and a constant width of  $w = 445$   $\mu\text{m}$  with the goal of producing a focus at a distance of 3 mm.

### Simulated Performance

From the modified THz rules of thumb (“Input Coupling”) and the output ring phase relations (“Output Coupling”), two single-sided lenses (SS1 and SS2) and one double-sided lens (DS1) were designed with identical input ring dimensions, as given in Table 2. The simulated transmission gain from the designed BE structure is shown in Fig. 7a along with the simulation computed for the actual dimensions of the fabricated devices.



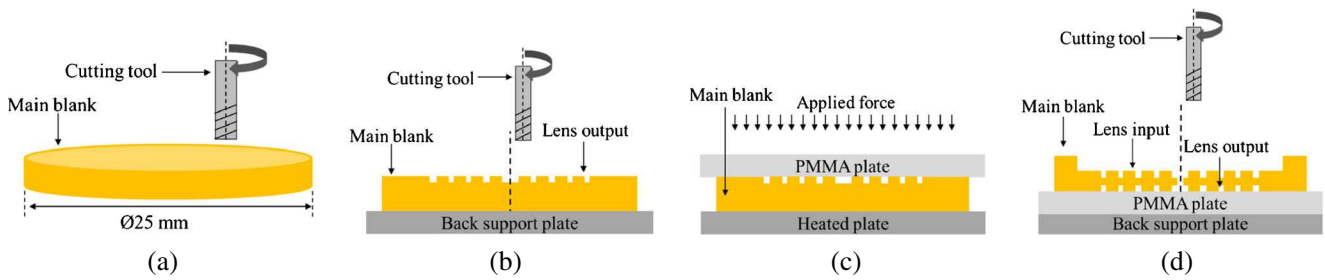
**Fig. 8** The Kugler Microgantry nano5X micromachining system. This modular, multi-functional unit is capable of fly cutting, micromilling, and micromachining

Figure 7b shows the simulated output beam profile for DS1. The position of the focus has been determined to be at a distance of 3.2 mm (Fig. 7c), in good agreement with the design phenomenological phase model discussed above.

### Fabrication

Fabrication of the BE lenses was accomplished using a Kugler Microgantry nano5X micromachining system (Fig. 8) in the National Research Council of Canada’s Automotive and Transportation Division [30]. The system integrates several micromachining technologies and measurement instrumentation and is capable of fabricating optical surface quality ( $R_a < 10$  nm) and high aspect ratio (1:280) components and performing advanced micromachining processes such as picosecond laser polishing.

The system uses three micromachining technologies: (1) fly cutting with a 2000 rpm spindle, (2) micromilling with an 180,000 rpm spindle, and (3) micromachining with a picosecond laser. A Renishaw touch probe with a measurement accuracy of  $\pm 500$  nm was used for measuring workpiece geometry before and after machining and during alignment. A Blum laser tool setting sensor with a measurement repeatability ( $2\sigma$ ) of 100 nm was used for measuring cutting tool geometry (e.g., diameter and overhang length). The system is equipped with an air-bearing motion stage with a position measuring resolution of 10 nm. The positioning accuracy is within  $\pm 250$  nm in the  $xy$ -direction and  $\pm 500$  nm in the  $z$ -direction. Straightness is within  $\pm 800$  nm per 500 mm travel for all linear axes. The system includes



**Fig. 9** The fabrication process flow for a double-sided BE lens (not to scale). **a** The main blank is fabricated with a diamond cutter. **b** The main blank is fixed and output rings are micromilled. **c** A PMMA hot-press process provides structural integrity. **d** The device is flipped and

input rings are micromilled. The final step involves electroplating a 1  $\mu\text{m}$  gold coating (not shown)

an automatic tool changer that is able to accommodate up to 60 cutting tools.

The design of the BE lens presented three main challenges for fabrication. First, accuracy on all dimensions was to be within  $\pm 10 \mu\text{m}$ . Second, precise axial alignment between both faces of the device was required since drilling the aperture is the last step in the process. Third, and most challenging, was to keep the thickness at the center of the lens as thin as possible to enhance throughput while maintaining structural integrity. The process flow used in the fabrication of the double-sided BE structure and is shown Fig. 9.

**Process Flow**

**Copper Blank** The first step involved fabricating a copper blank with a diameter of 25 mm and thickness of 3 mm while maintaining a plane and parallel device. This was performed by micromilling with a diamond flat cutter with a diameter of 2 mm, a rotational speed of 30,000 rpm, and a feed rate of 240 mm/min (Fig. 9a). The achieved thickness deviation was better than  $\pm 5 \mu\text{m}$  (with greater precision possible).

**Output Rings** The main blank was then fixed and circular channels with a rectangular cross-section were micromilled

on the output surface (Fig. 9b) with a flat end diamond cutter having a diameter of 300  $\mu\text{m}$ , a rotational speed of 30,000 rpm and feed rate of 120 mm/min, removing 20  $\mu\text{m}$  depth for each cutting path within a channel.

**Hot Embossing** The input surface was fabricated using a hot embossing process to provide structural integrity. (Fig. 9c). A 1-mm-thick PMMA plate was used as a die and placed between the output corrugations and a Crystal Digital Load Cell E-Z Press, which applies a controlled force and is equipped with temperature controlled heated platens. The platens were heated above PMMA glass transition temperature (107  $^{\circ}\text{C}$ ). The back supporting plate was made under 300 N force applied for a period of 10 min to ensure an accurate match with lens geometry.

**Input Rings** The input surface was micromilled using the same cutting parameters and machining strategy as used for the output surface (Fig. 9d). The final step was to electroplate a 1  $\mu\text{m}$  gold coating to avoid oxidation.

**Fabricated Lens Parameters**

An example of a BE lens fabricated using the technique described in Section “Process Flow” is shown Fig. 10. The left figure shows the input surface of the BE lens with

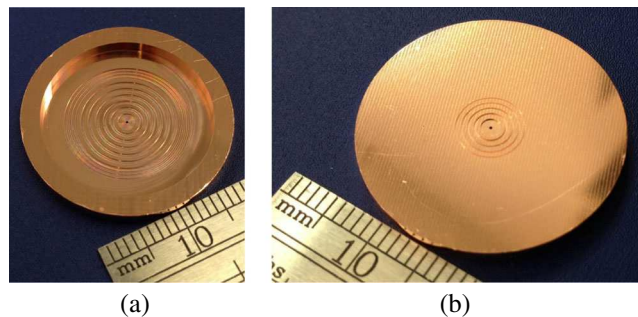


**Fig. 10** **a** Input side and **b** output side of the fabricated double-sided device, DS1

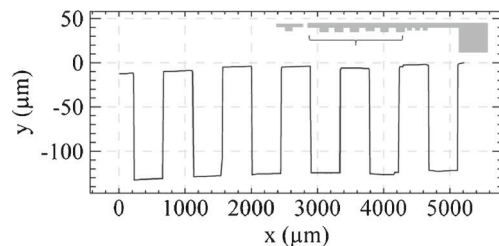


**Fig. 11** An example of input ring profile measurements obtained for SS2 showing feature accuracies better than 10  $\mu\text{m}$

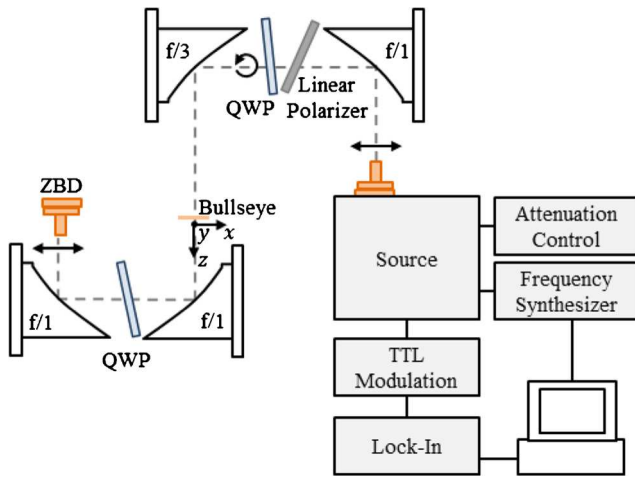


**Fig. 12** Schematic of the THz testbed used for transmission measurements. A predominately Gaussian, horizontally polarized, THz beam is produced by a VDI line source and is optically isolated using a QWP. Input optics ( $f/1$  and  $f/3$   $90^\circ$  OAP mirrors) collect the beam and produce an intermediate image plane ( $w_0 = 5.1$  mm) at the location of the BE lens. The output optics ( $f/1$  and  $f/1$   $90^\circ$  OAP mirrors) carry the beam through a second QWP before detection by the ZBD. For beam profile measurements, a knife-edge was cut through the intermediate focus

the integrated support ring, which allows for ease of handling. The Bragg grating can also be seen in this image. The right figure shows the radially tuned structures on the output surface of the lens which result in beam confinement, as discussed in Section “Output Coupling”.

Measurements of the diameter, period, width, and depth of the fabricated lenses were obtained using Veeco WYKO NT1100 Optical Profilometer with a resolution of 0.1 nm. Table 2 compares the designed and fabricated parameters. It can be seen that the micromachining technique is capable of fabricating the lens with accuracies typically within a few microns for the key parameters. Not unexpectedly, the accuracy decreases the thinner the substrate. At the

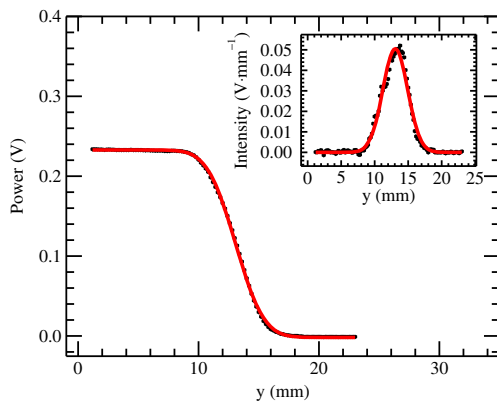


**Fig. 13** The measured (dotted) S-curve and error function fit (solid) at the location of the intermediate focus. Inset: the corresponding Gaussian beam profile and derivative of the error function fit

same time, the thinner lens results in greater transmission, as discussed in Section “Transmission Through the Aperture”. While a  $20\ \mu\text{m}$  thickness at the aperture location has been achieved, slight buckling of the substrate of  $\approx 10\ \mu\text{m}$  was observed, as shown in Fig. 11. To avoid buckling, this method may be adapted to fabricate a precision stainless steel mandrel that can be used to manufacture BE lenses using an embossing technique. To our knowledge, this is the first time a BE lens has been made using micromachining techniques.

### Experimental Configuration

To verify the performance of the fabricated BE lenses, an optical testbed consisting of a room temperature THz source and detector was developed, as shown schematically in Fig. 12. The source is a Virginia Diodes, Inc. (VDI) line source emitter, which can be tuned over the range of 320–330 GHz ( $908 - 937\ \mu\text{m}$ ) [31] and has a typical output power of  $\approx 10$  mW. We chose to operate the source at 330 GHz, where it produced a higher output power, while still remaining within the designed transmission resonance. The split-block diagonal feedhorn of the THz source emits a Gauss-Hermite beam with approximately 84.3 % of its power in the fundamental Gaussian mode [32]. At 330 GHz, the beam has a waist radius of 1.68 mm located 6.20 mm inside the feedhorn. Four diamond-turned, aluminum,  $90^\circ$  off-axis parabolic (OAP) mirrors were orientated in a “tip-to-tip” fashion such that rays from a single field point strike identical coordinates on each parabolic mirror [33]. A quartz quarter-wave plate (QWP) was placed in the collimated beam to act as an optical isolator. The BE lens under study is located at the intermediate focus and is mounted on a precision x-y-z translation stage for alignment. A second QWP located after the BE lens converts the circularly polarized beam to linear polarization for detection by a zero-biased diode (ZBD) detector. The ZBD has a diagonal feedhorn identical to that of the source. The

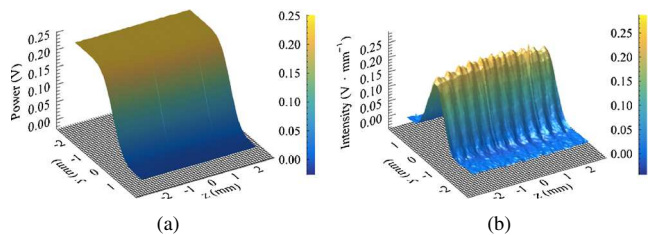


**Fig. 14** **a** The measurements the beam profile as the knife-edge is displaced along the optical axis. **b** The variation in the beam profile as a function of distance along the optical axis. As expected, the beam widens and the intensity drops away from the focus position. Variations in the peak amplitude are due to interference effects cause by ubiquitous resonant cavities, whose spacing corresponds  $\lambda/2$

**Table 3** A comparison of the theoretical and measured transmission gain,  $G_{theo}$  and  $G_{exp}$ , respectively, for the three BE lenses (Table 2) measured at a frequency,  $f$

	Incidence	$f$ (GHz)	Signal ( $\mu$ V)	$G_{exp}$	$G_{theo}$
SS1	Planar	329.500	$51.9 \pm 0.1$	–	–
SS1	Input	328.030	$1997 \pm 3$	$38.5 \pm 0.1$	$40 \pm 3$
DS1	Input	329.875	$1981 \pm 3$	$38.2 \pm 0.1$	$32 \pm 3$
SS2	Planar	329.453	$3.3 \pm 0.2$	–	–
SS2	Input	328.141	$89 \pm 1$	$27 \pm 2$	$38 \pm 3$

THz source was modulated by an external TTL source at a frequency of 1 kHz, and standard lock-in amplifier techniques were used to increase the signal-to-noise ratio.

**Incident Beam Profile**

Knife-edge measurements were conducted to verify the spatial profile the THz beam. A three-axis piezo driven stage allowed a thin blade to be translated through the beam at different distances from the focus. The blade could be positioned within 0.2  $\mu$ m in any direction. Control and data-acquisition software was written to translate the blade

(either horizontally,  $x$ , or vertically,  $y$ ) to successively block the beam and to record the measured signal from the lock-in amplifier as a function of the knife-edge position.

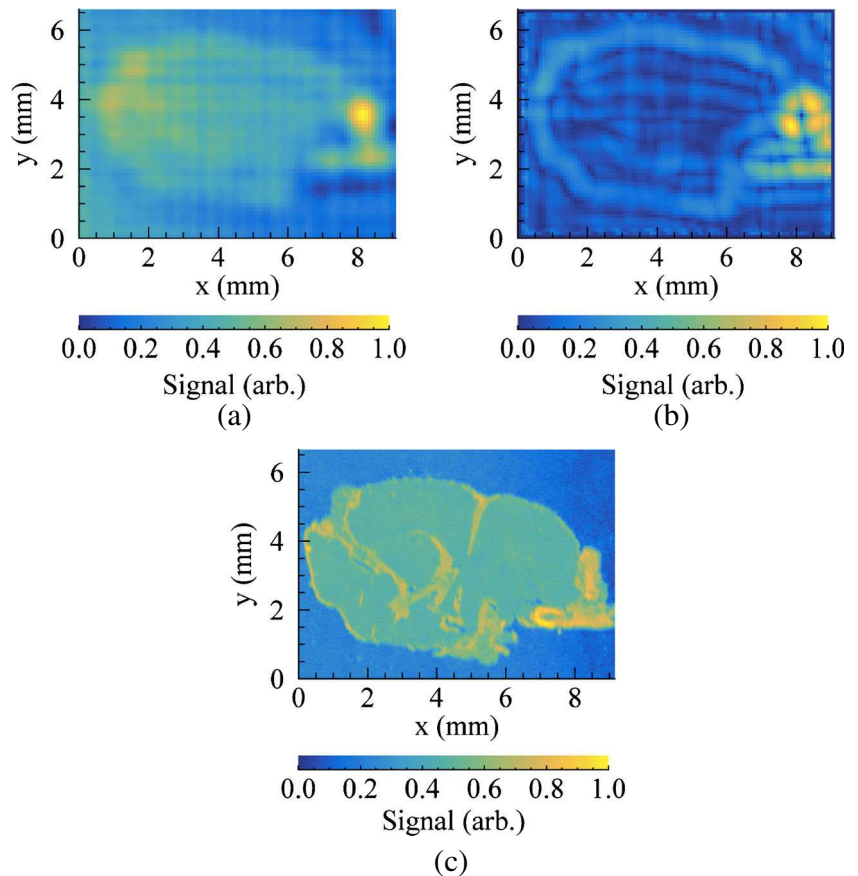
In the case of a Gaussian beam cut in the vertical direction,  $y$ , the signal takes the form of a S-curve error function [34],

$$P = \frac{P_T}{2} \left( 1 - \operatorname{erf} \left( \frac{\sqrt{2}(y - y_0)}{w_0} \right) \right), \tag{7}$$

which corresponds to the integrated beam intensity profile of the Gaussian beam. Error functions were fitted to the S-curves with a fixed total power,  $P_T$ , to obtain the Gaussian beam waist,  $w_0$ , and the optical axis,  $y_0$ .

Figure 13 shows the S-curve measured at the location of the focus. The derivative of the S-curve resulted in the Gaussian profile (inset). The scans were repeated as a function of  $z$  to study how the beam profile changes along the optical axis, as shown in Fig. 14. The location of the focus can be determined by finding the  $z$ -location corresponding to the minimum waist size. These results show that our THz testbed is producing a well-defined Gaussian beam of known width at the location of the plasmonic lens.

**Fig. 15** Images of paraffin-embedded rat brain. **a** THz image, **b** edge detection of the THz image with an applied Sobel filter, and **c** optical image of the same field



## Results

### Transmission Enhancement

The performance of the three fabricated BE lenses (Table 2) was verified by placing each device into the THz testbed, shown in Fig. 12. Each lens was illuminated with a Gaussian beam of waist radius of  $w_0 \approx 5.1$  mm. Standing waves in the testbed are unavoidable since all surfaces are reflecting at these wavelengths. Although care was taken to place absorbing material [35] over all of the non-active components, all measurements were taken at a fixed frequency of 330 GHz to minimize systematic errors.

The signal transmitted through SS1, SS2, and DS1 was recorded, and the measured transmission enhancement,  $G_{exp}$ , was determined by taking the ratio of these values with the signal transmitted through SS1 and SS2 with their planar side facing the incident beam, which is equivalent to the transmission through a single aperture. In each case, the measured error in  $G$  was approximately 1 %, dominated by the lower signal-to-noise ratio of the single-sided planar measurement. The results are summarized in Table 3. The measured enhanced transmission is in close agreement with that predicted by the theoretical model and to our knowledge is significantly higher than reported elsewhere in the literature [3, 11, 20, 36, 37].

### Subwavelength Imaging

To verify that we had obtained subwavelength imaging, DS1 was integrated into a THz imaging microscope with a configuration similar to that of the THz testbed shown in Fig. 12. The microscope was used to obtain images of paraffin-embedded rat brain. Figure 15a shows the raw THz image of the sample. In many studies of tissue samples, boundary determination is important. Figure 15b shows the boundary of the THz image determined by application of a Sobel filter [38], commonly used for this purpose. An optical image of the same field is shown in Fig. 15c for comparison.

These images and independent observations of a calibration target have been used to determine the spatial resolution of the THz microscope. The derived value of 338  $\mu\text{m}$  is in excellent agreement with the 300  $\mu\text{m}$  aperture of the BE lens, confirming that subwavelength imaging has been achieved.

## Conclusions

In this paper, we present the design, fabrication, and experimental performance of plasmonic lenses optimized for frequencies around 300 GHz. Theoretical modeling has

been used to derive rules of thumb for BE lenses at THz frequencies. These rules of thumb are similar to those proposed for use at visible wavelengths, but differ significantly due to differences in the permittivity of metals at longer wavelengths. Moreover, since most metals behave as perfect electrical conductors at THz frequencies, these rules of thumb are broadly applicable and independent of material choice. We have expanded previous work to include the design of structures on the output side of the lens to aid in beam confinement. Several BE lenses have been fabricated using a micromachining approach that is capable of producing lenses as designed with typical accuracies of less than 10  $\mu\text{m}$ . The lenses have been measured to have enhanced transmission gains of approximately 40, in excellent agreement with the theoretical model. The subwavelength spatial resolution has also been verified. The double-sided lens have been integrated into a  $xy$ -microscope translation stage and used to obtain images of paraffin-embedded rat brain. A preliminary comparison of the THz image with one obtained at optical wavelengths shows several common features.

The thinnest lens we have been able to manufacture successfully using the micromachining process outlined above are 20  $\mu\text{m}$ . We are currently exploring methods of micromachining a hardened steel mandrel and employing embossing techniques of thin metal films to create lenses of similar structure to that presented here on a thinner substrate. While models predict that the additional transmission gain is modest, being a factor of 2 for an aperture of  $d = 200$   $\mu\text{m}$  and 4 for an aperture of  $d = 100$   $\mu\text{m}$ , if successful, an embossing technique would lead to low cost fabrication of plasmonic lenses.

## References

1. Pickwell E, Wallace VP (2006) J Phys D 39(17):R301
2. Yin X, Ng BWH, Abbott D (2012) Terahertz imaging for biomedical applications, 1st edn. Springer, New York
3. Chiu CM, Chen HW, Huang YR, Hwang YJ, Lee WJ, Huang HY, Sun CK (2009) Opt Lett 34(7):1084
4. Born M, Wolf E (1999) Principles of optics. Cambridge University Press, Cambridge
5. Hunsche S, Koch M, Brener I, Nuss M (1998) Opt Commun 150:22
6. Bethe HA (1944) Phys Rev 66(7–8):163
7. Ebbesen TW, Lezec HJ, Ghaemi HF, Thio T, Wolff PA (1998) Nature 391:667
8. Degiron A, Ebbesen TW (2004) Opt Express 12(16):3694
9. Pellerin K, Lezec H, Ebbesen T, Linke R, Thio T (2001) In: Proceedings of the 2001 1st IEEE Conference on Nanotechnol., pp 293–298
10. Lezec HJ, Degiron A, Devaux E, Linke RA, Martín-Moreno L, García-Vidal FJ, Ebbesen TW (2002) Science 297:820
11. Ishihara K, Ichi Hatakoshi G, Ikari T, Minamide H, Ito H, Ohashi K (2005) Jpn J Appl Phys 44(32):L1005
12. Shi H, Du C, Luo X (2007) Appl Phys Lett 91(9):093111

13. Hao F, Wang R, Wang J (2010) *Plasmonics* 5(1):45
14. Raether H (1988) *Surface plasmons on smooth and rough surfaces and on gratings*. Springer, Berlin Heidelberg
15. Ru ECL, Etchegoin PG (2009) *Principles of surface-enhanced raman spectroscopy*. Elsevier, Amsterdam
16. Lumerical Solutions, Inc (2015) <http://www.lumerical.com/tcad-products/fdtd/>
17. Johnson PB, Christy RW (1972) *Phys Rev B* 6:4370
18. Ordal MA, Long LL, Bell RJ, Bell SE, Bell RR, Alexander RW, Ward CA (1983) *Appl Opt* 22(7):1099
19. Azad AK, Zhang W (2005) *Opt Lett* 30(21):2945
20. Baragwanath A, Freeman J, Gallant A, Zeitler J, Beere H, Ritchie D, Chamberlain M (2010) In: 35th international conference on infrared millimeter and terahertz waves, pp 1–2
21. Mahboub O, Palacios SC, Genet C, Garcia-Vidal FJ, Rodrigo SG, Martín-Moreno L, Ebbesen TW (2010) *Opt Express* 18(11):11292
22. Kraus JD, Carver KR (1973) *Electromagnetics*, 2nd edn. McGraw-Hill, New York
23. García-Vidal FJ, Martín-Moreno L, Lezec HJ, Ebbesen TW (2003) *Appl Phys Lett* 83(22):4500
24. Caglayan H, Bulu I, Ozbay E, *Opt J* (2006) *Soc Am B* 23(3):419
25. Kim S, Lim Y, Kim H, Park J, Lee B (2008) *Appl Phys Lett* 92(1):013103
26. Jia B, Shi H, Li J, Fu Y, Du C, Gu M (2009) *Appl Phys Lett* 94(15):151912
27. Wang J, Zhou W (2009) *Plasmonics* 4(3):231
28. Mote RG, Zhou W, Fu Y (2010) *Optik* 121(21):1962
29. Hao F, Wang R, Wang J (2010) *Plasmonics* 5(4):405
30. NRC Automotive and Surface Transportation (2015) <http://www.nrc-cnrc.gc.ca/eng/rd/ast/>
31. Virginia Diodes (2015) <http://vadiodes.com/>
32. Johansson JF, Whyborn ND (1991) *IEEE Trans on Microw Theory and Techn* 40(5):63
33. Malone RM, Becker SA, Dolan DH, Hacking RG, Hickman RJ, Kaufman MI, Stevens GD, Turley WD (2006) *Proc SPIE* 6288:62880Z
34. Dobroiu A, Yamashita M, Ohshima YN, Morita Y, Otani C, Kawase K (2004) *Appl Opt* 43(30):5637
35. Emerson & Cuming Microwave Products, Inc (2015) <http://www.eccosorb.com/>
36. Agrawal A, Cao H, Nahata A (2005) *Opt Express* 13(9):3535
37. Caglayan H, Bulu I, Ozbay E (2005) *Opt Express* 13(5):1666
38. Gonzalez R, Woods R (2008) *Digital image processing*. Pearson/Prentice Hall